




## Precise measurement of the configurational energy of bent graphene membranes via three-dimensional force field spectroscopy

Makoto Ashino <sup>1,2,\*</sup>, Keita Nishioka,<sup>1</sup> Keiji Hayashi <sup>1</sup> and Roland Wiesendanger <sup>2</sup>

<sup>1</sup>*Kanazawa Institute of Technology, Kanazawa 921-8501, Japan*

<sup>2</sup>*Department of Physics, University of Hamburg, Hamburg 20355, Germany*



(Received 3 May 2021; accepted 16 July 2021; published 6 August 2021)

Flexural deformations of atomically thin membranes are governed by bending rigidity and the Gaussian modulus. In one-atom-thick graphene membranes, these two parameters need to be determined via bending-induced changes in topology and interaction between electron orbitals, going beyond existing studies on flat graphene. Herein, we employ atomic force microscopy to demonstrate that the configurational (strain) energy can successfully be evaluated based on changes in the surface geometry with subatomic resolution via three-dimensional analyses of attractive interatomic forces. A quadratic relation of adhesion energy with monolayer curvatures of rolled and unrolled graphene led to the finding that the probe tip can detect spatially varying surface potentials owing to the rehybridization effects and the change in the next-neighbor hopping caused by bending. The tip-induced local strain inside graphene was found to generate topological defects, independently of in-plane stretch. Their energetic analysis and relationship with local curvatures reveal the applicability of the Helfrich Hamiltonian and determine the bending rigidity and Gaussian modulus. Those evaluated at the hollow sites of the honeycomb lattice are consistent with the isotropic elastic attributes. The remarkably large negative Gaussian modulus, observed at a pyramidalized carbon atom located at the topmost center of the tip-induced bump, provides evidence for attractive interactions between the charge inhomogeneity owing to the topological defects and geometric potentials of the Gaussian curvature.

DOI: [10.1103/PhysRevB.104.085407](https://doi.org/10.1103/PhysRevB.104.085407)

### I. INTRODUCTION

Membranes [1] are composed of extremely thin two-dimensional (2D) sheets. Because thermal energy can hardly stretch but easily bend the membranes, they are considered to be nonstretchable despite being highly flexible. Cell membranes [2] are quasi-2D “fluid” sheets of lipid bilayers, and flexural events of fission and fusion are ubiquitous in cell biology [3]. Graphene [4] is a one-atom-thick 2D crystalline sheet, representing a prototypical “solid” membrane. However, it is susceptible to flexural deformations such as ripples [5], bubbles [6,7], buckles [8–11], wrinkles [12], crumples [13], scrolls, and folds [14,15]. The flexural “spontaneous” deformations are regarded as inconveniences to be prevented or mitigated [16]. However, the curved configurations and their interplays with other physical and chemical properties have given rise to entirely new research fields with versatile applications [17], ranging from strained semiconductors [18] to drug delivery, structural composites, ultrasensitive nanoelectromechanical systems, such as pressure, gas, and mass sensors [19–21], frequency resonators [8,22,23], thermoelectromechanical nanodevices [9], and thermal-energy harvesters [10,24]. These applications, accompanied by controlling and manipulating the flexural deformations, require the understanding of their mechanics and energetic relationship with curvatures.

The isotropic 2D membrane is modeled as a structureless continuum surface (arbitrary 2D manifolds [25,26]). Its configurational energy without long-range order is described using the Helfrich Hamiltonian as follows [27,28]:

$$\varepsilon = \int_S \left( \epsilon + \frac{1}{2} \kappa_b C_T^2 + \kappa_G C_G \right) dS, \quad (1)$$

where  $C_T = 1/R_1 + 1/R_2$  is the total curvature (the sum of two local principal curvatures:  $1/R_1$ ,  $1/R_2$ ), and  $C_G = (1/R_1)(1/R_2)$  is the Gaussian curvature. Parameters  $\epsilon$ ,  $\kappa_b$ , and  $\kappa_G$  are the energy for a unitary flat surface, bending rigidity, and the Gaussian modulus, respectively [3,29,30]. Because the fluid membrane lacks long-range order,  $\kappa_b$  has been well estimated via experiments and simulations [3], following Eq. (1), wherein the  $\kappa_G$  term vanishes owing to the Gauss-Bonnet theorem [31]. A typical  $\kappa_b$  of lipid bilayers is  $(5\text{--}25)k_B T$ , which is small enough when compared with the thermal energy scale of membranes that undulate or fluctuate noticeably at physiological temperatures [1,3].

In contrast, the solid membranes might require consideration of long-range contributions, predominantly in-plane stretching elasticity. Multilayer graphene of thickness  $t$  follows the classical plate theory [32], where  $\kappa_b$  and  $\kappa_G$  are given by 2D Young's modulus  $Y_{2D}$  (and Poisson's ratio  $\nu$ ) as  $\kappa_b = Y_{2D} t^2 / 12(1 - \nu^2)$  and  $\kappa_G = -(1 - \nu) \kappa_b = -Y_{2D} t^2 / 12(1 + \nu)$  [32,33], respectively. The second term in Eq. (1) (bending energy per area) yields  $\varepsilon_b = Y_{2D} (t C_T)^2 / 24(1 - \nu^2)$ . Even when  $Y_{2D}$  is extremely large,  $(t C_T)^2 \leq 10^{-6}$  reduces  $\varepsilon_b$  ( $\kappa_b$ ) to reasonably smaller values. However, for one-atom-thick

\*Corresponding author: [mashino@neptune.kanazawa-it.ac.jp](mailto:mashino@neptune.kanazawa-it.ac.jp)

graphene, the classical plate theory leads to an unrealistically high Young's modulus  $Y$ , and thickness  $t$  even smaller than the diameter of a carbon atom [34,35]. Alternatively,  $Y_{2D}$  ( $= Yt$ ) has been vigorously evaluated via experiments and simulations, following a theory for nonlinear mechanics of membranes [6,36,37], where  $\kappa_b$  is modeled as "zero" (negligible). Coupling between bending deformations and the in-plane stretch is believed to stabilize even noticeable thermal undulations or fluctuations. This so-called membrane theory considers the deformations requiring energy comparable to  $Y_{2D}$ , which is three orders of magnitude larger than the thermal energy [37].

Within the thermal energy scale ( $\sim k_B T$ ), not only  $\kappa_b$  but also  $\kappa_G$  contributes to the flexural "spontaneous" deformations such as ripples, bubbles, buckles, wrinkles, and crumples in the graphene membranes as well as fission and fusion events in the cell membranes. However, for one-atom-thick graphene,  $\kappa_b$  is still poorly specified and far from being fully understood. Parameter  $\kappa_b$  needs to be determined via bending-induced changes in interactions between electron orbitals [35,38–40]; however, the existing methods studied  $\kappa_b$  only on flat graphene [41,42]. Moreover, characterizing  $\kappa_G$  is extremely difficult even for fluid membranes. The Gauss-Bonnet theorem [31] states that the integral of  $C_G$  over the surface without any boundary is invariant under any deformation that does not involve topological transformations. Furthermore,  $\kappa_G$  has little effect at equilibrium when curvature fluctuations occur at constant topology [43–46]. Therefore, it is necessary to either introduce a boundary or change the topology via individual deformations to obtain the experimental signals directly sensitive to  $\kappa_G$  [3]. Although shape changes in such specified samples as vesicles with phase coexistence [47] have been utilized for fluid membranes, topology manipulation has not yet been applied to fluid and solid membranes. Besides, on a solid membrane, it is also difficult to discriminate  $C_G$  from its geometric coupling with an in-plane stretch. Consequently, only a few computational estimates have been proposed to date; however these estimates contradict one another [29,30,44].

In this study, we report the technical details on a direct measurement of the inherent values of  $\kappa_b$  and  $\kappa_G$  of monolayer graphene [48]. We applied 3D force field spectroscopy (3D-FFS) [49], based on atomic force microscopy (AFM) [50,51], to convex-curved graphene [52] in rolled and unrolled forms such as carbon nanotubes (CNTs) of various radii, and a bent graphene nanoribbon (BNR) with locally variable curvature. The overall radii of CNTs and the local curvature variations of BNR were measured via AFM imaging with high precision. The force-spectra analysis revealed that the curvature-dependent changes in surface potentials were equivalent to the configurational (or strain) energy without a long-range order (free from surface tension). A quadratic relationship between adhesion energy and the curvature forms the basis of a successful extraction of  $\kappa_b$ , independent of the rolled and unrolled forms. We found that the tip-induced local strains inside graphene generate topological defects [53], geometrically decoupling  $C_G$  from the in-plane stretch. Subatomic 3D analyses of the surface potentials during the bump creation and their relationship with  $C_G$  realized the first direct determination of  $\kappa_G$ . The attractive interaction [53] between the

tip-induced topological defects at the pyramidalized carbon atoms [54] on top of the bump and the geometric potentials of  $C_G$  explains its remarkably large negative values.

## II. SAMPLES AND AFM IMAGING TO DETERMINE THEIR CURVATURES

Single-walled CNTs were synthesized by arc discharge and heated in air to open their ends [55]. Their radial breathing modes in Raman spectroscopy indicated relatively broad distributions of discrete peaks for radii of 0.63–0.65 nm, 0.74–0.75 nm, 0.81–0.84 nm, and 0.90–0.92 nm. They were dispersed, together with the reference tubes (0.69  $\pm$  0.01 nm) [56], into an SDS solution and deposited onto a highly doped Si substrate covered by atomically flat dry-SiO<sub>2</sub> films. After transfer into ultrahigh vacuum (UHV), the sample was heated to remove the solvent and other adsorbates. The experiments were performed using our home-built UHV low-temperature AFM optimized for atomic-scale studies [57] and a commercial silicon cantilever with a monocrystalline-Si tip [58]. Operation temperature and pressure were  $T < 15$  K and  $p < 1 \times 10^{-8}$  Pa, respectively. After transfer into vacuum, the tip was cleaned by Ar<sup>+</sup> sputtering. The contact potential differences were compensated by applying bias voltages to minimize long-range electrostatic forces [51]. Dynamic-mode operation [59] of the cantilever with spring constant  $k_c = 34.3$  N/m and oscillation amplitudes  $A = 2.1$ – $2.3$  nm prevented jump-to-contact and other instabilities. Extremely low damping assured tip-apex stabilities during all experiments and high reproducibility of our results owing to the high sensitivity to atomic-scale tip-apex changes [60].

High-resolution AFM topographies on CNTs [Figs. 1(a)–1(d)] indicated no "ghost structures" caused by double or multiple tips. The widths and asymmetries of sections could be affected by the tip-apex shape. By deconvoluting the topographies [61] on the reference tubes [56] [Fig. 1(c)], the tip-apex radius was evaluated to be  $R_t \cong 0.58$  nm. With such an atomically sharp tip, sensing short-range attractive interatomic forces made it possible to visualize true surface topographies on van der Waals surfaces, independently of their in-plane elasticities [62]. By comparing the topographic heights on CNTs [Figs. 1(a), 1(b) and 1(d)] with those on the reference tubes ( $R_0^{\text{CNT}} = 0.69 \pm 0.01$  nm) [Fig. 1(c)], their original radii were determined to be  $R_0^{\text{CNT}} = 0.81$  nm, 0.75 nm, and 0.65 nm (with  $< 3.8\%$  standard deviation). The accuracy was confirmed by the the chiral indices derived from a combination of Raman spectroscopy [55] and atomic-resolution AFM [63].

The attractive interatomic forces between the tip-apex atom and the atomically specific sites of the sample surface provide atomic-scale contrast [49,63]. The topographic minima and maxima in Figs. 1(e)–1(h) are assigned to the hexagonal carbon lattice and hollow sites, respectively [49,64]. The topographic maxima in the upper panels have six nearest neighbors separated approximately by the lattice parameter ( $a = 0.246$  nm) in the tube-axis directions, but elongated by 25%–60% in their orthogonal directions. The elongation of atomic-scale features is explained geometrically by assuming a pointlike tip scanning across a curved surface [65]. As depicted in the lower panels, the corrected images almost

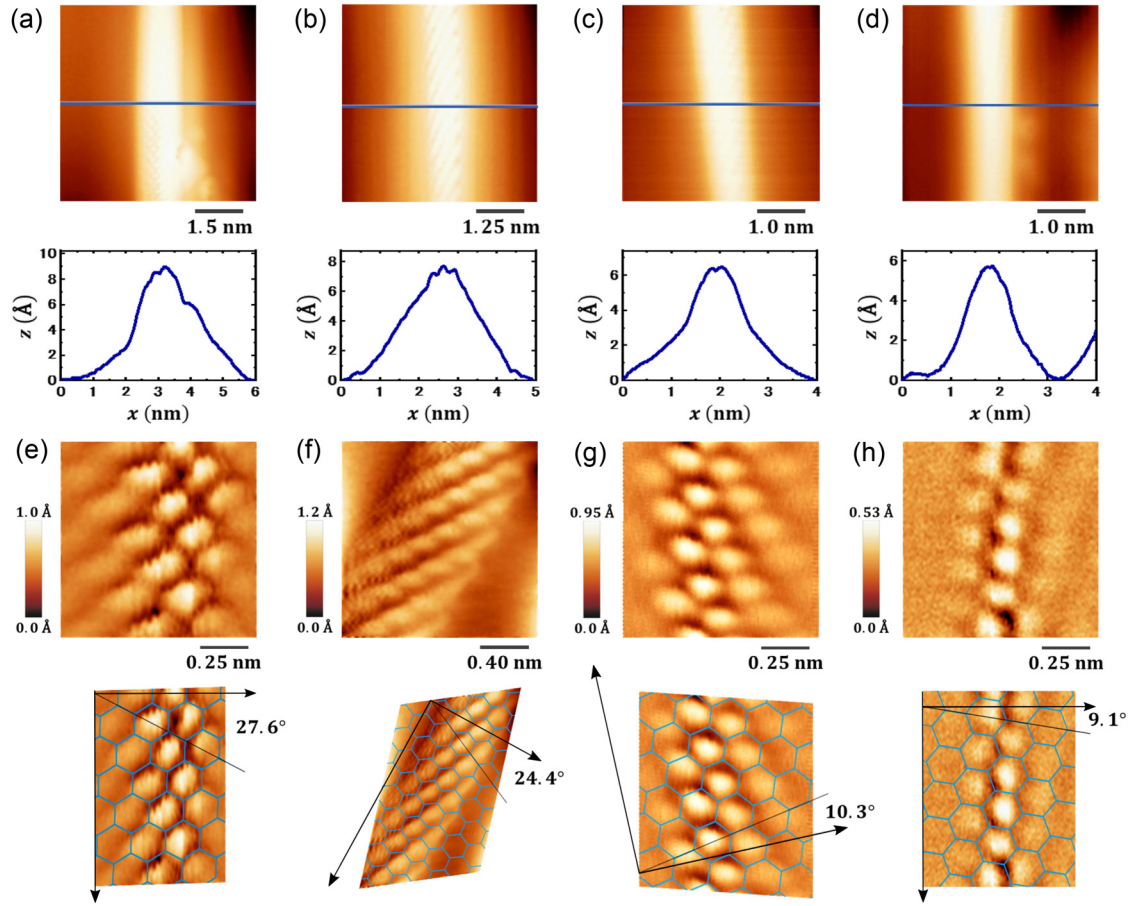


FIG. 1. AFM topographies (2D) of CNTs with different  $R_0^{\text{CNT}}$ , obtained under feedback control to keep (a)  $\Delta f = -52.8$  Hz, (b)  $-63.8$  Hz, (c)  $-99.0$  Hz, and (d)  $-101$  Hz of the resonant oscillation ( $f_0 \cong 159$  kHz) and a bias voltage ( $U_{\text{bias}} = 0.30$  V) applied to the cantilever. The section along a horizontal line is respectively displayed below. (e)–(h) The closed-up images (upper), respectively from the centers of (a)–(d). The corrected images (bottom) fit the honeycomb graphene lattice of  $a = 0.246$  nm and the chiral angles  $\phi$ .

represent a 0.246-nm separation in every direction. A pair of indices  $(n, m)$  of CNTs is determined via their relationships with chiral angle  $\phi$  and  $R_0^{\text{CNT}}$ :

$$\phi = \arccos \left[ \frac{\sqrt{3}(n+m)}{2\sqrt{n^2+m^2+nm}} \right], \quad (2)$$

$$R_0^{\text{CNT}} = \frac{a}{2\pi} \sqrt{n^2+m^2+nm}. \quad (3)$$

The chiral indices in Fig. 1(e) with  $\phi = 27.6^\circ$  and  $R_0^{\text{CNT}} = 0.81$  nm, Fig. 1(f) with  $\phi = 24.4^\circ$  and  $R_0^{\text{CNT}} = 0.75$  nm, Fig. 1(g) with  $\phi = 10.3^\circ$  and  $R_0^{\text{CNT}} = 0.69$  nm, and Fig. 1(h) with  $\phi = 9.1^\circ$  and  $R_0^{\text{CNT}} = 0.65$  nm were identified to be (20, 1), (2, 18), (7, 13), and (12, 7), respectively. These results are consistent with those of the synthesized CNTs (semiconducting) [55] and the reference tubes (metallic) [56].

A 3D view of AFM topography [Fig. 2(a)] indicates that the protruding part, exhibiting atomically superimposed helical features, corresponds to the sidewall of a  $R_0^{\text{CNT}} = 0.69$  nm nanotube [see atomistic model (right)]. Figure 2(b) was obtained at the location of the reference tubes. However, the atomically superimposed helical features are visible over the whole area in Fig. 2(b) having the same  $3 \times 3$  nm<sup>2</sup> size as Fig. 2(a). Because the radial breathing modes indicate  $R_0^{\text{CNT}} \leq$

0.93 nm, we conclude that the atomic features in Fig. 2(b) correspond to the sidewall of an unrolled tube. Most likely, a reference tube got accidentally unzipped along its axis [66] and became a BNR, as modeled (right). In the topography [Fig. 2(c)] obtained after tilting, the atomic features are observed even near the right-hand edge of the BNR. Therefore, the edges would be tightly fixed to the oxidized substrate.

### III. FORCE SPECTRA ANALYSES VIA 3D FORCE FIELD SPECTROSCOPY

In 3D-FFS for CNTs,  $20 \times 20 \times 512$  to  $30 \times 30 \times 512$  data points were individually captured during the tip retraction in nominally  $1.0 \times 1.0 \times 3.0$  nm<sup>3</sup> boxes over the topmost centers. For the BNR, the capturing center was arranged at a midline position between lines (ii) and (iii) by tilting the sample stage [Fig. 2(c)]. Consequently, this procedure prevented vacancy defects from the capturing box (insets of Fig. 4). Immediately after the acquisition of the atom-resolved topography [Fig. 2(c)],  $30 \times 50 \times 512$  data points were captured during the tip retraction in a nominal  $1.5 \times 2.5 \times 3.0$  nm<sup>3</sup> box. The  $z$ -height images simultaneously obtained [67] obviously exhibited atomic-scale contrast (insets of Figs. 3 and 4) after being extrapolated to  $10 \times 10$  times larger pixel numbers



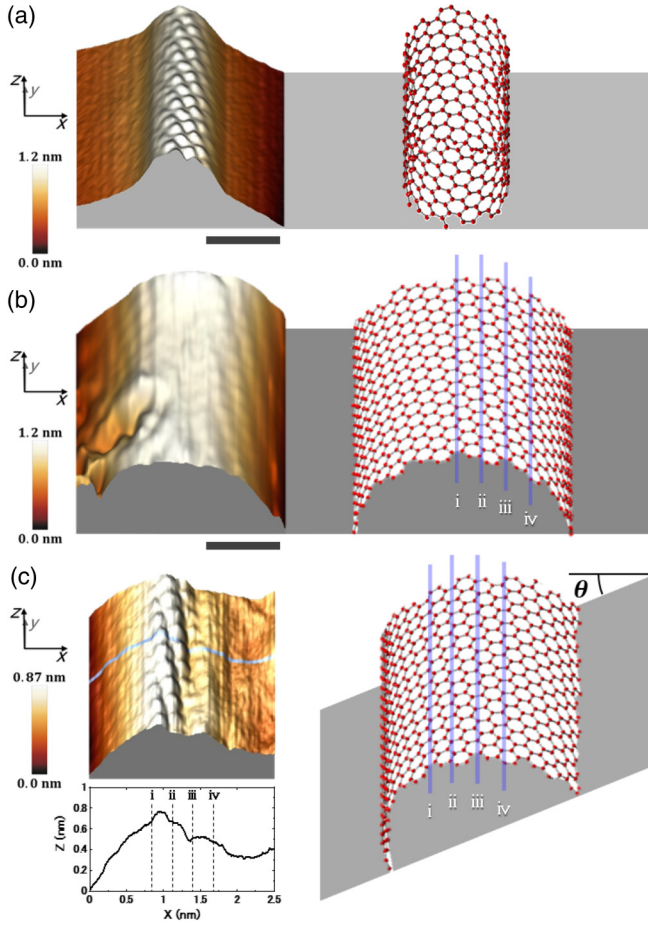


FIG. 2. AFM topographies (3D) with atomically superimposed helical features obtained under feedback control to maintain (a)  $\Delta f = -98.2$  Hz ( $U_{\text{bias}} = 0.30$  V) for CNT and (b)  $-128$  Hz and (c)  $-129$  Hz ( $U_{\text{bias}} = 0.23$  V) for BNR. The scale bar is 1 nm. A line section of (c) is displayed in the bottom. The atomistic models of a single-walled nanotube of helical index (13,7) and bent nanoribbons unzipped along the  $y$  axis from a (13,7) nanotube are illustrated on the right. The topmost centers in (b) and (c) respectively correspond to line (i) and midway between lines (ii) and (iii) because the sample stage was tilted by a certain angle  $\theta$  in (c).

than the raw data. Their comparison with the atom-resolved AFM topographies obtained just beforehand (afterward) made it possible to assign the individual force spectrum to the hollow (HL) and carbon-atom (C) sites of the honeycomb lattice.

The interatomic forces  $F_{\text{int}} \equiv F_{\text{HI}}^{\text{CNT}}$  and  $F_{\text{C}}^{\text{CNT}}$  ( $F_{\text{HI}}^{\text{BNR}}$  and  $F_{\text{C}}^{\text{BNR}}$ ) [67] are plotted as open- and closed-color dots, respectively, in the upper panels of Figs. 3(a)–3(d) for CNTs [Fig. 4(a)–4(d) for BNR]. They were obtained by separately averaging multiple spectra at two different equivalent sites (HI and C sites) over the topmost  $0.3 \times 1.0$  nm<sup>2</sup> of CNTs (Fig. 1) [along lines (i)–(iv) on BNR (Fig. 2)]. The differences between  $F_{\text{HI}}^{\text{CNT}}$  and  $F_{\text{C}}^{\text{CNT}}$  evidently depend on  $R_{\text{O}}^{\text{CNT}}$  [52]. Indeed, Fig. 3(c) represents almost the same features as those obtained for another tube of  $R_{\text{O}}^{\text{CNT}} = 0.69 \pm 0.01$  nm [56] even on the HOPG substrate with another Si-cantilever tip [49,63]. Particularly,  $F_{\text{C}}^{\text{CNT}}$  at C sites exhibited strong correlations with  $R_{\text{O}}^{\text{CNT}}$ , as depicted in Fig. 3, where  $F_{\text{C}}^{\text{CNT}}$  (closed

dots) evidently become stronger for smaller  $R_{\text{O}}^{\text{CNT}}$ . This result can be attributed to the  $\pi$ - $\sigma$  rehybridization stimulated by the reduction in the C-C bond angles [54,68] owing to bending distortions of the curved graphene monolayers.

To analyze the atomically site-specific relationships of  $F_{\text{int}}$  with local curvature  $1/R$ , we follow the method proposed in [68] based on the potential functions  $U_{\text{int}}^{sp^2}$  and  $U_{\text{int}}^{sp^3}$  for carbon atoms with  $sp^2$  and  $sp^3$  hybridization, respectively. This method drives new parameters for the bond orbitals  $h_{\pi}$  ( $\pi$  states acquiring a small  $\sigma$ -orbital component) in the  $\pi$ - $\sigma$  rehybridization by introducing a curvature parameter  $g(1/R)$ . Interatomic potential  $U_{\text{int}}$  is expressed as a function of  $1/R$  in addition to interval  $z_{\text{int}}$  between the tip-apex atom and the closest atomic site of graphene, as follows:

$$U_{\text{int}}(1/R, z_{\text{int}}) = g(1/R)U_{\text{int}}^{sp^2}(z_{\text{int}}) + [1 - g(1/R)]U_{\text{int}}^{sp^3}(z_{\text{int}}), \quad (4)$$

where  $g(1/R)$  is defined as

$$g(1/R) = \left(1 - \frac{1/R}{1/R_t}\right)^{\eta}. \quad (5)$$

The Lennard-Jones (L-J) and Morse potentials were utilized, respectively, as  $U_{\text{int}}^{sp^2}$  and  $U_{\text{int}}^{sp^3}$ :

$$U_{\text{int}}^{sp^2}(z_{\text{int}}) = U_{\text{O}}^{sp^2} \left[ \left(\frac{z_{\text{O}}}{z_{\text{int}}}\right)^{12} - 2\left(\frac{z_{\text{O}}}{z_{\text{int}}}\right)^6 \right], \quad (6)$$

$$U_{\text{int}}^{sp^3}(z_{\text{int}}) = U_{\text{O}}^{sp^3} \left\{ \exp\left[-2\left(\frac{z_{\text{int}} - z_{\text{O}}}{\lambda}\right)\right] - 2 \exp\left[-\left(\frac{z_{\text{int}} - z_{\text{O}}}{\lambda}\right)\right] \right\}. \quad (7)$$

By differentiating Eqs. (4), (6), and (7),  $F_{\text{int}}$  was obtained as follows:

$$F_{\text{int}}(1/R, z_{\text{int}}) = g(1/R)F_{\text{int}}^{sp^2}(z_{\text{int}}) + [1 - g(1/R)]F_{\text{int}}^{sp^3}(z_{\text{int}}), \quad (8)$$

$$F_{\text{int}}^{sp^2}(z_{\text{int}}) = \frac{12U_{\text{O}}^{sp^2}}{z_{\text{O}}} \left[ \left(\frac{z_{\text{O}}}{z_{\text{int}}}\right)^{13} - \left(\frac{z_{\text{O}}}{z_{\text{int}}}\right)^7 \right], \quad (9)$$

$$F_{\text{int}}^{sp^3}(z_{\text{int}}) = \frac{2U_{\text{O}}^{sp^3}}{\lambda} \left\{ \exp\left[-2\left(\frac{z_{\text{int}} - z_{\text{O}}}{\lambda}\right)\right] - \exp\left[-\left(\frac{z_{\text{int}} - z_{\text{O}}}{\lambda}\right)\right] \right\}, \quad (10)$$

where decay length  $\lambda$  was individually estimated to obtain an excellent fit. Furthermore,  $1/R_t \equiv 1.724$  nm<sup>-1</sup> [Eq. (5)] was based on  $R_t \cong 0.58$  nm, and  $U_{\text{O}}^{sp^2} \equiv 10.2$  meV [Eq. (9)] and  $U_{\text{O}}^{sp^3} \equiv 1.41$  eV [Eq. (10)] correspond to the L-J parameter between Si and C atoms, estimated from that between two Ar atoms [69] and the Si-C binding energy on the graphene surface [70], respectively. The out-of-plane stiffness of monolayer graphene [30,52] is at least one order of magnitude smaller than that of the monocrystalline-Si tip ( $Y_{\text{Si}} = 180$  GPa) [71]. Because the attractive interatomic force  $F_{\text{int}}$  is expected to induce an out-of-plane displacement  $z_{\perp}$  in the topmost carbon atoms,  $z_{\text{int}}$  is described as  $z_{\text{int}} = z - z_{\perp}$  [Figs. 3(e) and 4(e)]. A superior agreement with all experimental plots at C sites of CNTs (Fig. 3) was obtained by setting  $\eta \equiv 0.027$  in Eq. (5) and changing  $z_{\perp}$  [right panel of Fig. 3(f)]. For HI sites, only

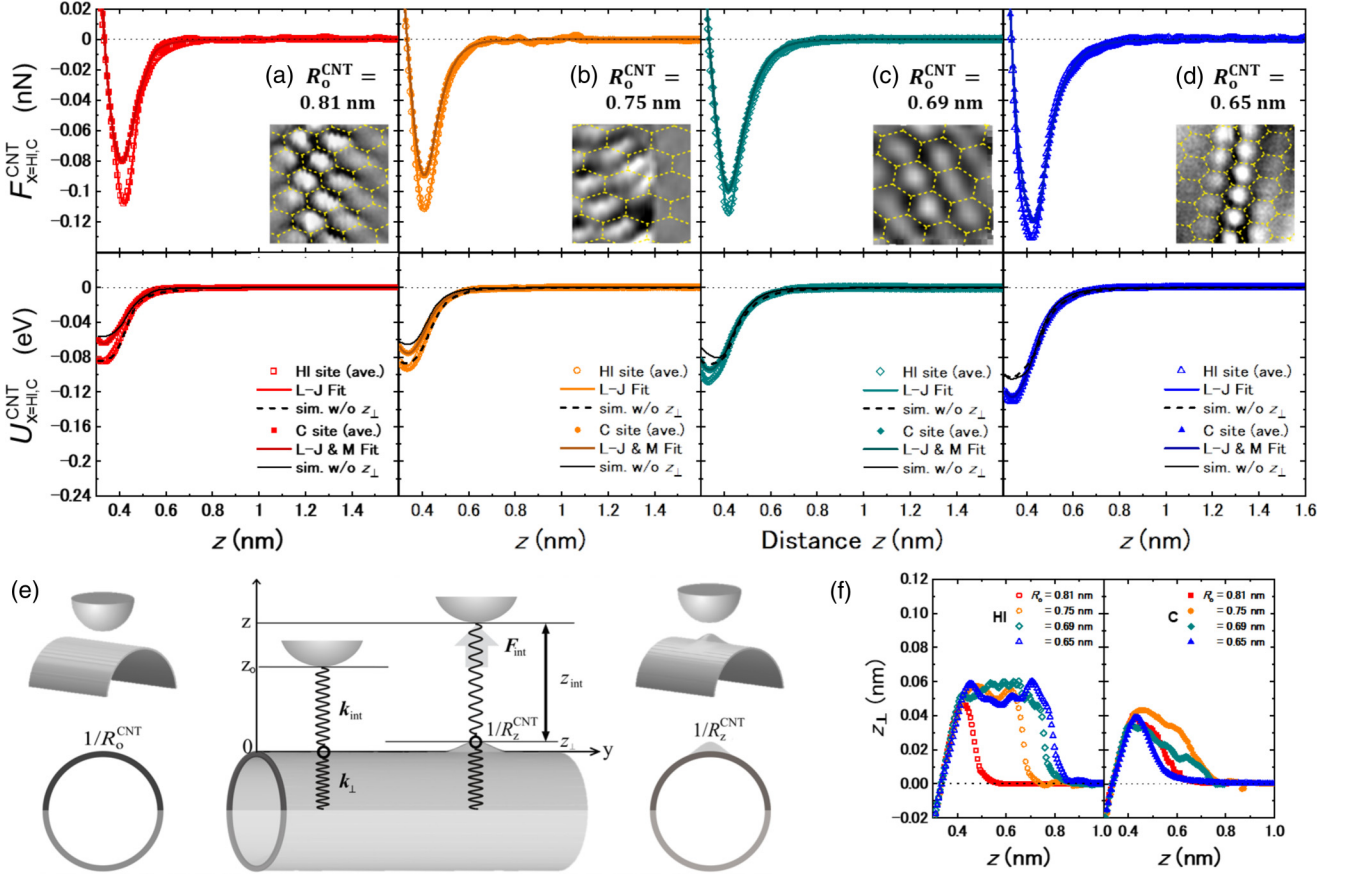


FIG. 3. Interatomic forces  $F_{int}$  (upper) and potentials  $U_{int}$  (lower) over CNTs of (a)  $R_o^{CNT} = 0.81$  nm, (b)  $0.75$  nm, (c)  $0.69$  nm, and (d)  $0.65$  nm. The open and closed dots correspond to hollow (HI) and carbon atom (C) sites, respectively. Each plot is arranged such that  $F(z) = 0$  should be at the equilibrium  $z_o = 0.335$  nm. Solid curves: Simulations using the Lennard-Jones (L-J) and Morse (M) potentials. Insets:  $z$ -height images ( $1.0 \times 1.0$  nm $^2$ ), extrapolated to  $400 \times 400$  pixels, on which the distorted honeycomb lattice is depicted. (e) Schematics of the surfaces with (right) and without (left) bump of height  $z_{\perp}$  [ $k_{\perp}$ ,  $k_{int}$ : out-of-plane elastic stiffness,  $F_{int} = k_{\perp}z_{\perp} = k_{int}(z_{int} - z_{\perp})$ ]. (f) The out-of-plane displacement  $z_{\perp}$  at HI (left) and C (right) sites of CNTs with different  $R_o^{CNT}$ .

$F_{int}^{sp^2}$  in Eq. (9) was utilized to obtain excellent fits, resulting in  $z_{\perp}$  variations (left panel). In a first-order approximation, even for CNTs within  $1/R_o < 2$  nm $^{-1}$  [72], the shape and net area of a six-membered ring remain the same as those for completely flat graphene. Because  $1/R = 0$  yields  $g(0) = 1$ , Eq. (8) is also applicable for HI sites.

Interatomic potentials  $U_{int} \equiv U_{HI}^{CNT}$  and  $U_C^{CNT}$  ( $U_{HI}^{BNR}$  and  $U_C^{BNR}$ ) are plotted as open- and closed-color dots, respectively, in the lower panels of Figs. 3(a)–3(d) for CNTs [Figs. 4(a)–4(d) for BNR]. The simulations using the same parameters as those for  $F_{int}$  but with and without  $z_{\perp}$  variations are described as colored and black lines, respectively. The dashed-black curves (HI sites of CNTs) indicate that their absolute maxima, i.e., the well depths  $U_o^{sp^2}$  of L-J potentials, increase with  $1/R_o^{CNT}$ . Furthermore,  $U_o^{sp^2} \equiv E_{HI}^{CNT}$  (adhesion energy) vs  $(1/R_o^{CNT})^2$  is plotted as open-blue dots in Fig. 5(a). Their linear fit (dashed-blue line) indicates a quadratic relationship between  $E_{HI}^{CNT}$  and  $1/R_o^{CNT}$ . The 3D view of AFM topography on BNR [Fig. 2(b)] and its cross sections [67] indicate that the topmost center slightly deforms inward. The locations of lines (i)–(iv), in which  $F_{int}$  ( $U_{int}$ ) plots (Fig. 4) were obtained, are aligned in the  $x$  direction perpendicular to the bending

axis. We infer that  $U_o^{sp^2} \equiv E_{HI}^{BNR}$  has a quadratic relationship with its local curvature  $1/R_{xo}^{BNR}$ , explicitly varying in the  $x$  direction. The maximum and minimum  $1/R_{xo}^{BNR}$  [lines (i) and (iv)] were first evaluated by fitting the sections of AFM topographies to those expected for semicylindrical surfaces with specified curvatures. The quadratic relationship of  $E_{HI}^{BNR}$  with  $1/R_{xo}^{BNR}$  was then applied to determine the remaining  $R_{xo}^{BNR}$  values [lines (ii) and (iii)]. Those procedures yielded  $R_{xo}^{BNR} \sim 1.32$  nm [line (i)], 1.24 nm [line (ii)], 1.18 nm [line (iii)], and 1.13 nm [line (iv)] with  $<6\%$  standard deviation. These  $R_{xo}^{BNR}$  values with all the parameters for CNTs provided excellent fits to the experimental plots of  $F_{HI}^{BNR}$  and  $U_{HI}^{BNR}$ , resulting in the  $z_{\perp}$  variations (Fig. 4). The slope of the dashed-red line in Fig. 5(a), drawn under the inference, corresponds approximately to that for CNTs (dashed-blue line).

#### IV. EXTRACTION OF BENDING RIGIDITY

Figures 3 and 4 depict that the contribution of the long-range order is negligible because the energy ( $\ll 1$  eV) is three orders of magnitude smaller than the energy from in-plane strain ( $\gg 10^3$  eV) [36]. At the equilibrium ( $z_o = 0.335$  nm)

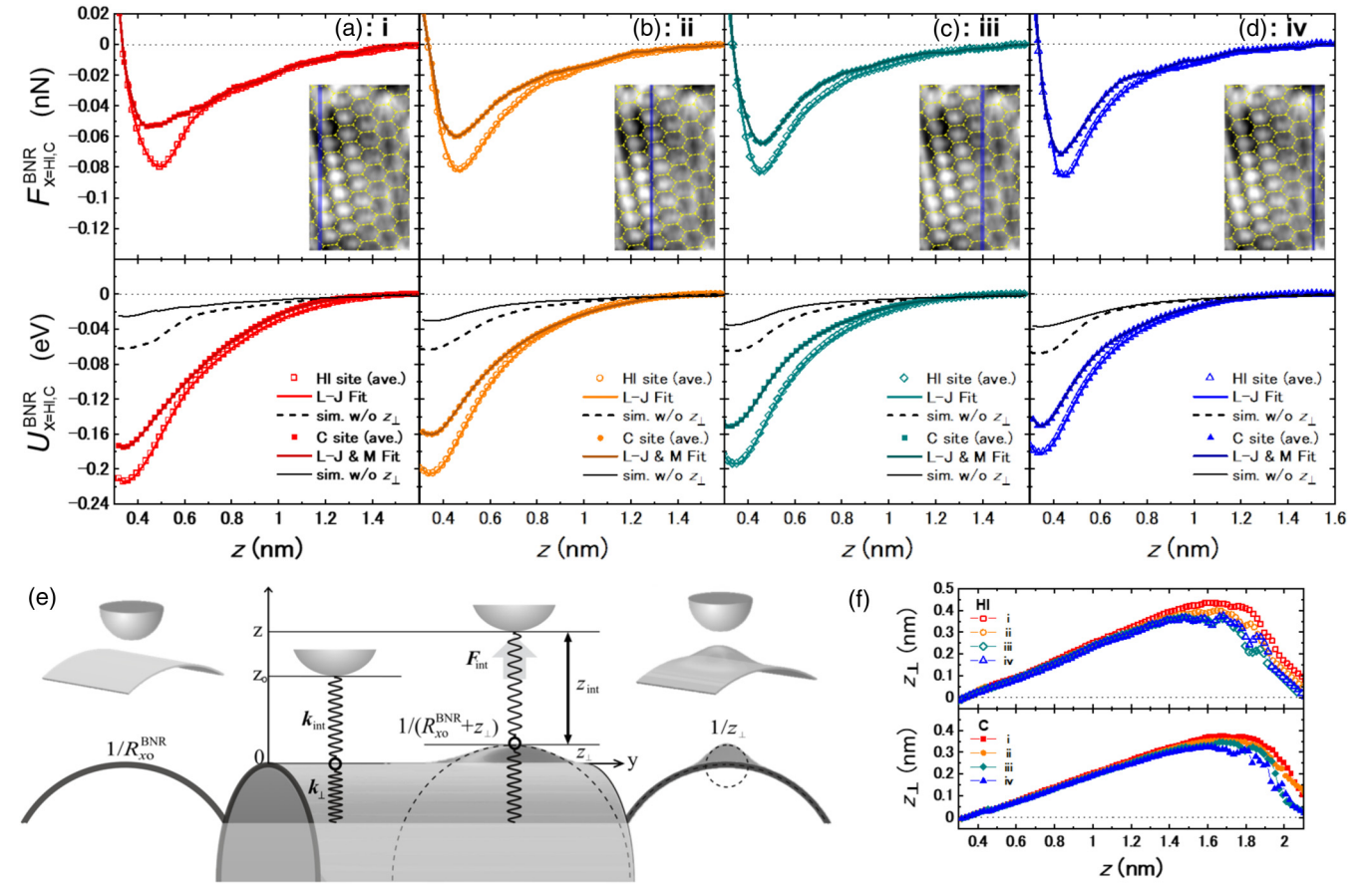


FIG. 4. Interatomic forces  $F_{int}$  (upper) and potentials  $U_{int}$  (lower) along line (i): (a), line (ii): (b), line (iii): (c), and line (iv): (d) over BNR. The open and closed dots correspond to HI and C sites, respectively. Each plot is arranged such that  $F(z) = 0$  should be at the equilibrium  $z_0 = 0.335$  nm. Solid curves: Simulations using the Lennard-Jones (L-J) and Morse (M) potentials. Insets:  $z$ -height images ( $1.5 \times 2.5$  nm<sup>2</sup>), extrapolated to  $300 \times 500$  pixels, on which the distorted honeycomb lattice is depicted. (e) Schematics of the surfaces with (right) and without (left) bump of height  $z_{\perp}$  [ $k_{\perp}$ ,  $k_{int}$ : out-of-plane elastic stiffness,  $F_{int} = k_{\perp} z_{\perp} = k_{int}(z_{int} - z_{\perp})$ ]. (f) The out-of-plane displacement  $z_{\perp}$  at HI (left) and C (right) sites along lines (i)–(iv) of BNR.

distance,  $F_{int}(z_0) = 0$  and thereby  $z_{\perp} = 0$  yields  $C_T = 1/R_0$  and  $C_G = 0$ . The configurational energy per atom is extracted from Eq. (1):

$$\varepsilon_0 = \varepsilon_0^{2D} + \frac{1}{2} S_0 \kappa_b \left( \frac{1}{R_0} \right)^2, \quad (11)$$

where  $\varepsilon_0^{2D}$  is the energy per atom for “completely flat” graphene, and  $S_0 = 3\sqrt{3}a_{cc}^2/4$  ( $= 0.0263$  nm<sup>2</sup>) is the planar footprint of a carbon atom in graphene with C-C bond length  $a_{cc} = 0.142$  nm [30]. From an atomistic view [left halves of Fig. 5(b)], the configurational (or strain) energy attributed to the bending distortions is dominated by adjustment of hopping integrals between the misaligned bond orbitals  $h_{\pi}$  in the  $\pi$ - $\sigma$  rehybridizations [35,73]. Herein, we assume that the increases in  $E_{HI} \equiv E_{HI}^{CNT}$  and  $E_{HI}^{BNR}$  at HI sites with  $(1/R_0)^2$  in Fig. 5(a) are equivalent to the increase in  $\varepsilon_0$  at  $z = z_0$  (i.e.,  $\Delta E_{HI} = \Delta \varepsilon_0$ ). Consequently, from Eq. (11), the slopes of the linear fits (dashed lines) are given by  $S_0 \kappa_b / 2$ , and  $\kappa_b$  is extracted as listed in Fig. 5(c). Indeed,  $[\kappa_b]_{HI}^{BNR} = 1.45 \pm 0.07$  eV indicates an excellent agreement with 1.44 eV [30] and 1.46 eV [38], derived from density functional theory, whereas  $[\kappa_b]_{HI}^{CNT} = (1.55 \pm 0.16)$  eV agrees well with 1.6 eV

[29,35] from density-functional-based tight-binding calculations. The most-cited  $\kappa_b = 1.2$  eV was deduced indirectly from the phonon spectrum of bulk graphite [41]. The excellent agreement between our experimental results for monolayer graphene and the theoretical calculations surely justifies the above assumption. Importantly, the configurational (or strain) energy was determined via the change in the adhesion energy inside the six-membered rings of the honeycomb graphene lattice. This finding means that the probe tip did detect the adjustment of the hopping integrals between the misaligned bond orbitals  $h_{\pi}$ . The areas inside the six-membered rings exhibited the isotropic elastic attributes of the monolayer [35], in which the framework of the Helfrich Hamiltonian (the quadratic curvature-elastic continuum theory) [27] was available.

For the C sites of CNTs (BNR), the absolute maxima of the simulations without  $z_{\perp}$  (solid-black curves) in the lower panels of Figs. 3(a)–3(d) and Figs. 4(a)–4(d) correspond to adhesion energy  $E_C$  (well depths of the hybrid of L-J and Morse potentials).  $E_C^{CNT}$  ( $E_C^{BNR}$ ) vs  $(1/R_0^{CNT})^2$  [ $(1/R_0^{BNR})^2$ ] is plotted as closed-blue (red) dots in Fig. 5(a). Their linear fits (solid blue and red lines), almost matching each other, indicate a quadratic relationship. Thereby, the increase in



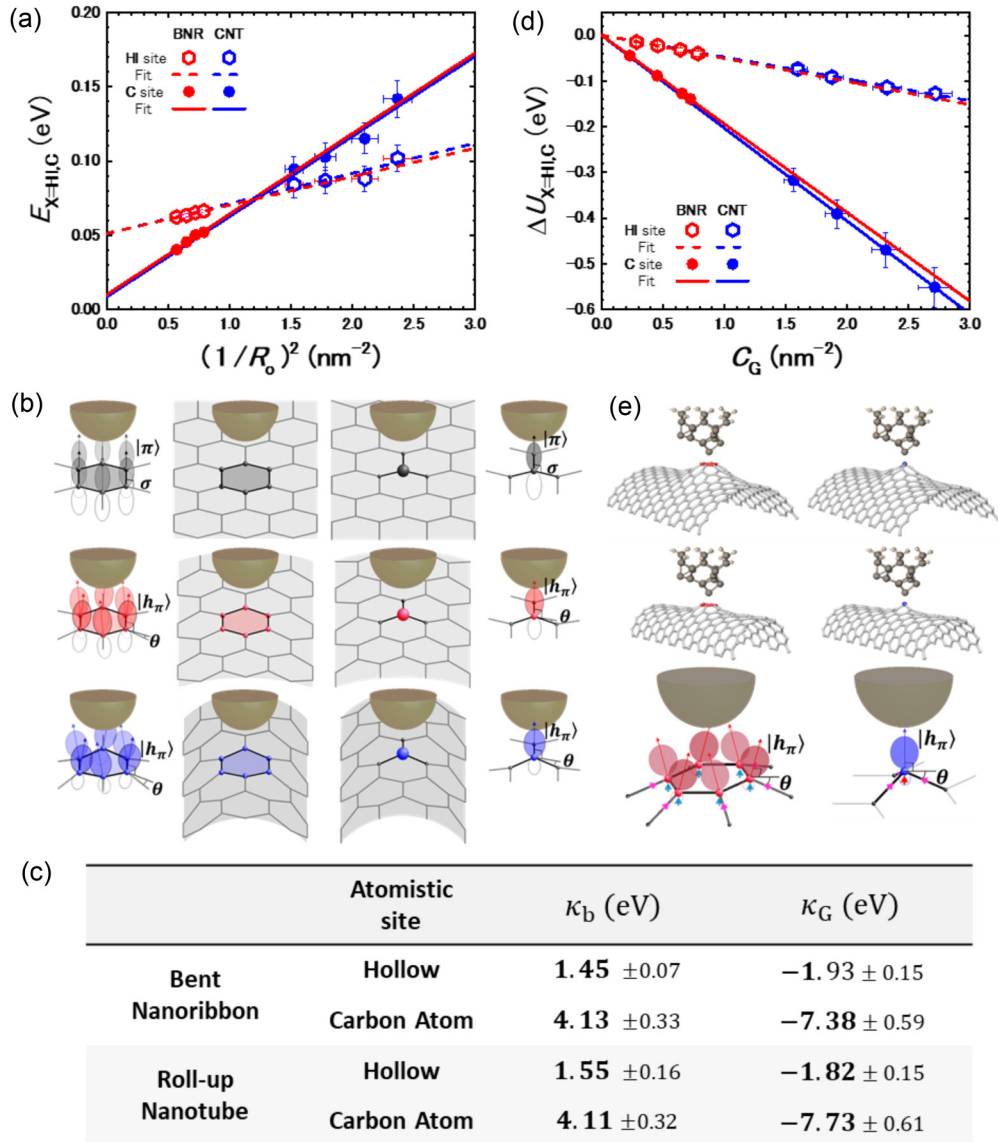


FIG. 5. (a) Adhesion energy versus square of original curvature at HI (open) and C sites (closed dots) of CNTs (blue) and BNR (red). (b) Schematic relationships of the tip-apex atom with HI (left) and C sites (right) of the completely flat (top), slightly bent (middle), and considerably bent (bottom) graphene. The interactions between the tip-apex atom and the  $h_\pi$  orbitals with the pyramidalization angle  $\theta$  and the  $\pi$ -orbital axis vectors (POAVs; upward arrows) are illustrated. (c) Bending rigidity and the Gaussian modulus, obtained via spectral analysis. (d) Lift-up energy of C atoms versus the Gaussian curvature at HI (open) and C sites (closed dots) of CNTs (blue) and BNR (red). (e) Simulations of bumps' creations triggered by attractive interactions of the tip-apex atom with HI (left) and C (right) sites of BNR (upper) and CNT (middle). Close-up diagrams of interactions between the tip-apex atom and the  $h_\pi$  orbitals with  $\theta$  and POAVs (upward arrows).

$E_C$  with  $(1/R_0)^2$  is assumed to be equal to the increase in  $\varepsilon_0$  at  $z = z_0$  ( $\Delta E_C \equiv \Delta \varepsilon_0$ ). Because the slopes of the solid lines steeper than the dashed lines (for HI sites) are also given by  $S_0 \kappa_b / 2$  [Eq. (11)],  $[\kappa_b]_C^{\text{CNT}} = 4.11 \pm 0.32$  eV and  $[\kappa_b]_C^{\text{BNR}} = 4.13 \pm 0.33$  eV were extracted for C sites of CNTs and BNR [Fig. 5(c)], respectively. From Eqs. (4) and (5),  $E_C$  is calculated as  $E_C = g(1/R_0)U_0^{sp^2} + [1 - g(1/R_0)]U_0^{sp^3}$ , where  $g(1/R_0)$  increasingly reduces with  $1/R_0$ . Consequently, the higher  $\kappa_b$  at C sites is found to result from the fact that the increase of  $1/R_0$  locally enhances the contributions of  $U_0^{sp^3}$ , attributed to the chemically radical  $\sigma$  state of a dangling bond following  $sp^3$  hybridization [see right halves in Fig. 5(b)] [52,74]. Therefore, we conclude that the config-

urational (strain) energy was measured via spatially varying surface potentials owing to the rehybridization effects and the change in the next-neighbor hopping caused by the bending curvatures.

The  $\kappa_b$  values directly obtained so far for monolayer graphene were  $\kappa_b = 7.1 \pm 3$  eV from the snap-through behavior of buckled configuration [11] and  $\kappa_b = 10^3 - 10^4$  eV from measuring spring constants of thermally fluctuating graphene cantilevers. Their variations by so many orders of magnitude indicate that direct measurement of  $\kappa_b$  has indeed been challenging for monolayer graphene. The following phenomena are thought to make the apparent value of  $\kappa_b$  so disparate in scale: The thermal fluctuations and static wrinkles can notably

TABLE I. Original curvatures  $1/R_{x_0}^{\text{BNR}}$  and geometric parameters  $\alpha$  (dimensionless) at the hollow (HI) and carbon-atom (C) sites of bent graphene nanoribbons.

$R_{x_0}^{\text{BNR}}$ (nm)	$1.32 \pm 0.07$	$1.24 \pm 0.07$	$1.18 \pm 0.06$	$1.13 \pm 0.06$
$1/R_{x_0}^{\text{BNR}}$ ( $\text{nm}^{-1}$ )	$0.762 \pm 0.042$	$0.806 \pm 0.044$	$0.849 \pm 0.047$	$0.889 \pm 0.049$
$[\alpha]_{\text{HI}}$	$0.218 \pm 0.015$	$0.218 \pm 0.015$	$0.225 \pm 0.016$	$0.254 \pm 0.018$
$[\alpha]_{\text{C}}$	$0.147 \pm 0.010$	$0.255 \pm 0.017$	$0.346 \pm 0.024$	$0.340 \pm 0.024$

stiffen the graphene membrane by effectively thickening the membrane, similar to how a crumpled sheet of paper is more rigid than a flat one [75]. The drastic increases in the local curvatures of multiple buckles and wrinkles inside the graphene membrane can individually stimulate the  $\pi$ - $\sigma$  rehybridization [52], resulting in its overall considerable reinforcement.

### V. EXTRACTION OF THE GAUSSIAN MODULUS

The lower panels in Figs. 3(a)–3(d) and Figs. 4(a)–4(d) depict that the absolute maxima of open-colored plots ( $|U_{\text{int}}|_{\text{max}}$  for HI sites) are evidently greater than the absolute maxima of the dashed-black curves (adhesion energy  $E_{\text{HI}}$ ). The differences ( $|U_{\text{int}}|_{\text{max}} - E_{\text{HI}}$ ) are thought to result from the fact that  $|U_{\text{int}}|_{\text{max}}$  includes the energy to pull the topmost carbon atoms upward and to create the bumps with  $C_{\text{T}} = 1/R_1 + 1/R_2$  and  $C_{\text{G}} = (1/R_1)(1/R_2)$  [Figs. 3(e) and 4(e)]. The difference ( $|U_{\text{int}}|_{\text{max}} - E_{\text{HI}}$ ) divided by the ratio of the effective area  $S_{\Omega}$  to  $S_0$  corresponds to the configurational energy per atom of the bump [Eq. (1)]:

$$\varepsilon_{\Omega} = \Delta\epsilon + \frac{1}{2}S_0\kappa_{\text{b}}C_{\text{T}}^2 + S_0\kappa_{\text{G}}C_{\text{G}}, \quad (12)$$

where  $\Delta\epsilon$  is an energy offset between  $|U_{\text{int}}|_{\text{max}}$  and  $\varepsilon_0$ . As depicted in Fig. 3(e), the bump on CNTs can be approximated as a semisphere of  $C_{\text{G}}^{\text{CNT}}$ , described with coefficient  $\beta$  [52] as follows:

$$C_{\text{G}}^{\text{CNT}} = \left( \frac{1}{R_0^{\text{CNT}}} + \beta z_{\perp} \right)^2 \equiv \left( \frac{1}{R_z^{\text{CNT}}} \right)^2. \quad (13)$$

The atomistic models of the bumps with respect to the tip-apex atom [middle row in Fig. 5(e)] indicate that  $S_{\Omega}$  can be approximated as  $S_0$  owing to the relatively smaller  $R_0^{\text{CNT}}$  (larger  $1/R_0^{\text{CNT}}$ ). For the HI sites of CNTs ( $\kappa_{\text{b}} = 1.55 \pm 0.16$  eV),  $\Delta U_{\text{HI}}^{\text{CNT}} \equiv \varepsilon_{\Omega} - \Delta\epsilon - \frac{1}{2}S_0\kappa_{\text{b}}C_{\text{T}}^2 (= S_0\kappa_{\text{G}}C_{\text{G}})$  as a function of  $C_{\text{G}} = (1/R_z^{\text{CNT}})^2$  is plotted as open-blue dots in Fig. 5(d). Because the slopes of the linear fits (dashed-blue line) to the  $\Delta U_{\text{HI}}^{\text{CNT}}$  plots are expressed as  $S_0\kappa_{\text{G}}$ ,  $[\kappa_{\text{G}}]_{\text{HI}}^{\text{CNT}} = -1.82 \pm 0.15$  eV was extracted [Fig. 5(c)].

Figure 4 depicts that  $z_{\perp}$  reached  $\approx 0.43$  nm (33% of  $R_0$ ) within the thermal energy scale ( $\ll 1$  eV). This result indicates that a bent graphene monolayer is insensitive to in-plane tensile strain, meaning that the geometric coupling of  $C_{\text{G}}$  with the in-plane stretch is negligible. The energy ( $\gg 10^3$  eV) from the in-plane stiffness is three orders of magnitude larger than the energy from bending [36]. Consequently, a bump having relatively wider skirts would be locally created, accompanying the out-of-plane displacements of the surrounding atoms without changing the original base curvature  $1/R_{x_0}^{\text{BNR}}$  [see Figs. 4(e) and 5(e)]. Hence,  $C_{\text{G}}^{\text{BNR}}$  can be straightforwardly

approximated as a product of two local-principal curvatures with dimensionless parameter  $\alpha$  (Table I):

$$C_{\text{G}}^{\text{BNR}} = \alpha \left( \frac{1}{R_{x_0}^{\text{BNR}} + z_{\perp}} \right) \left( \frac{1}{z_{\perp}} \right). \quad (14)$$

The atomistic models of the bumps on BNR with respect to the tip-apex atom [upper row in Fig. 5(e)] indicate that, when the C and HI sites are located at their top-most center,  $S_{\Omega}$  can be approximated, respectively, as  $1.5S_0$  and  $3S_0$  owing to their relatively larger  $R_{x_0}^{\text{BNR}}$  (smaller  $1/R_{x_0}^{\text{BNR}}$ ). For the HI sites of BNR ( $\kappa_{\text{b}} = 1.45 \pm 0.07$  eV),  $\Delta U_{\text{HI}}^{\text{BNR}} \equiv \varepsilon_{\Omega} - \Delta\epsilon - \frac{1}{2}S_0\kappa_{\text{b}}C_{\text{T}}^2 (= S_0\kappa_{\text{G}}C_{\text{G}})$  as a function of  $C_{\text{G}} = \alpha[1/(R_{x_0}^{\text{BNR}} + z_{\perp})](1/z_{\perp})$  is plotted as open-red dots in Fig. 5(d). The slopes ( $S_0\kappa_{\text{G}}$ ) of the linear fits (dashed-red line) to the  $\Delta U_{\text{HI}}^{\text{BNR}}$  plots yields  $[\kappa_{\text{G}}]_{\text{HI}}^{\text{BNR}} = -1.93 \pm 0.15$  eV [Fig. 5(c)].

The lower panels in Figs. 3(a)–3(d) and Figs. 4(a)–4(d) also depict that the absolute maxima of closed-colored plots ( $|U_{\text{int}}|_{\text{max}}$  for C sites) are evidently greater than the absolute maxima of solid-black curves (adhesion energy  $E_{\text{C}}$ ). The difference ( $|U_{\text{int}}|_{\text{max}} - E_{\text{C}}$ ) can determine the energy  $\varepsilon_{\Omega}$  to create the bumps of  $C_{\text{G}}$ . Hence,  $\Delta U_{\text{C}}^{\text{CNT}}$  and  $\Delta U_{\text{C}}^{\text{BNR}} \equiv \varepsilon_{\Omega} - \Delta\epsilon - \frac{1}{2}S_0\kappa_{\text{b}}C_{\text{T}}^2 (= S_0\kappa_{\text{G}}C_{\text{G}})$  for the C sites of CNTs ( $\kappa_{\text{b}} = 4.11 \pm 0.32$  eV) and BNR ( $\kappa_{\text{b}} = 4.13 \pm 0.33$  eV) are plotted as functions of  $C_{\text{G}} = (1/R_z^{\text{CNT}})^2$  and  $C_{\text{G}} = \alpha[1/(R_{x_0}^{\text{BNR}} + z_{\perp})](1/z_{\perp})$  in closed-blue and red dots, respectively. However, the linear fits (solid lines) to the  $\Delta U_{\text{C}}^{\text{CNT}}$  and  $\Delta U_{\text{C}}^{\text{BNR}}$  plots with significantly larger negative slopes ( $S_0\kappa_{\text{G}}$ ) than those ( $S_0\kappa_{\text{G}}$ ; dashed lines) for HI sites yield remarkably large negative values:  $[\kappa_{\text{G}}]_{\text{C}}^{\text{CNT}} = -7.73 \pm 0.61$  eV for CNTs and  $[\kappa_{\text{G}}]_{\text{C}}^{\text{BNR}} = -7.38 \pm 0.59$  eV for BNR [Fig. 5(c)].

In our study,  $\kappa_{\text{G}}$  was almost independent of whether the rolled or unrolled forms of graphene were considered (free from surface tension). This is in agreement with the finding that  $C_{\text{G}}$  can be geometrically decoupled from the in-plane stretch for one-atom-thick graphene. In contrast, the obvious difference in  $\kappa_{\text{G}}$  between HI and C sites may simply result from the significant contribution of the Morse potentials at the C site (the local stimulation of  $h_{\pi}$ ). However, Figs. 3 and 4 depict that  $F_{\text{int}}$  ( $\approx 0.12$  nN maximum) is still significantly smaller than that of chemical forces (usually  $> 1$  nN [51]). Indeed,  $F_{\text{int}}$  at the vacancy defects (see Fig. 2) attained values significantly larger than 1 nN. Although the curvature-induced stimulation of the  $\pi$ - $\sigma$  rehybridization caused a significant increase of  $\kappa_{\text{b}}$  at C sites, such high  $\kappa_{\text{b}}$  prevented the formation of larger bumps. Figure 4(f) indicates that the amplitudes of the bumps at C sites, reaching up to  $z_{\perp} \approx 0.37$  nm (28% of  $R_0$ ) at the maximum for BNR, are smaller than those at the HI sites ( $z_{\perp} \approx 0.43$  nm, 33% of  $R_0$ ).



As depicted in Fig. 5(e), the strains induced at C sites by the attractive interatomic forces of the tip-apex atom align along three main  $\langle 100 \rangle$  crystallographic directions whereas those at HI sites are isotropic. Those strains at C sites enhance so-called pyramidalization, in which three nearest neighbors are no longer planar but located in the corners of pyramids [54]. Such a nonuniform (threefold) strain field acting as a topological defect can eliminate the band degeneracy, and that locally lifted degeneracy restores band mass to the electrons and possibly even renders the topmost area of the bumps electrically insulating [76]. Thereby, the charge inhomogeneity (or pointlike  $h_\pi$  stimulation) can arise at the topological defects of C sites. In the presence of the topological defects,  $C_G$  can have a significantly direct consequence by introducing an effective gauge field [73]. The charge inhomogeneity (or bond orbitals  $h_\pi$  owing to the  $\pi$ - $\sigma$  rehybridizations) locally stimulated by the pyramidalization of the topmost carbon atoms of the bumps can interact attractively with the geometric potentials of  $C_G$ . Therefore, such an anomalous coupling between the topological defects and geometric potentials [53] might work as a driving force to create bumps and explain why  $\kappa_G$  attains the remarkably large negative values.

## VI. CONCLUSIONS

We quantitatively studied the attractive interatomic interactions between the opposing atoms of AFM tip apex

and atomically specific sites of a graphene monolayer. The force-spectra analysis revealed that the configurational (strain) energy was precisely measured via the AFM tip that evidently detected spatially varying surface potentials owing to the rehybridization effects and the change in the next-neighbor hopping caused by the bending curvatures. The quadratic relationship between adhesion energy and curvature ensures a successful extraction of  $\kappa_b$ , independent of the rolled and unrolled forms. The tip-induced local strains inside graphene monolayers were found to create topological defects, geometrically decoupling  $C_G$  from the in-plane stretch. A subatomic 3D analysis of the surface potentials during the creation of the bump as well as their relationship to  $C_G$  realized a direct determination of  $\kappa_G$ . The attractive interaction between the topological defects induced at the pyramidalized carbon atoms on top of the bump and the geometric potentials of  $C_G$  is most probably responsible for the remarkably large negative values of  $\kappa_G$ .

## ACKNOWLEDGMENTS

The authors gratefully acknowledge Dr. F. Simon for supplying the files to create atomistic models. This work was partially supported by JSPS KAKENHI Grant No. JP18K05047.

- 
- [1] D. Nelson, T. Piran, and S. Weinberg, *Statistical Mechanics of Membranes and Surfaces* (World Scientific, 2004).
- [2] D. Boal and D. H. Boal, *Mechanics of the Cell* (Cambridge University Press, 2012).
- [3] M. Hu, J. Briguglio, and M. Deserno, *Biophys. J.* **102**, 1403 (2012).
- [4] K. S. Novoselov, D. Jiang, F. Schedin, T. J. Booth, V. V. Khotkevich, S. V. Morozov, and A. K. Geim, *Proc. Natl. Acad. Sci. USA* **102**, 10451 (2005).
- [5] A. Fasolino, J. H. Los, and M. I. Katsnelson, *Nat. Mater.* **6**, 858 (2007).
- [6] P. Wang, W. Gao, Z. Cao, K. M. Liechti, and R. Huang, *J. Appl. Mech.* **80**, 040905 (2013).
- [7] K. Yue, W. Gao, R. Huang, and K. M. Liechti, *J. Appl. Phys.* **112**, 083512 (2012).
- [8] P. Xu, M. Neek-Amal, S. D. Barber, J. K. Schoelz, M. L. Ackerman, P. M. Thibado, A. Sadeghi, and F. M. Peeters, *Nat. Commun.* **5**, 3720 (2014).
- [9] M. Neek-Amal, P. Xu, J. K. Schoelz, M. L. Ackerman, S. D. Barber, P. Thibado, A. Sadeghi, and F. M. Peeters, *Nat. Commun.* **5**, 4962 (2014).
- [10] M. L. Ackerman, P. Kumar, M. Neek-Amal, P. M. Thibado, F. M. Peeters, and S. Singh, *Phys. Rev. Lett.* **117**, 126801 (2016).
- [11] N. Lindahl, D. Midtvedt, J. Svensson, O. A. Nerushev, N. Lindvall, A. Isacson, and E. E. B. Campbell, *Nano Lett.* **12**, 3526 (2012).
- [12] W. Bao, F. Miao, Z. Chen, H. Zhang, W. Jang, C. Dames, and C. N. Lau, *Nat. Nanotechnol.* **4**, 562 (2009).
- [13] R. J. T. Nicholl, N. V. Lavrik, I. Vlassioux, B. R. Srijanto, and K. I. Bolotin, *Phys. Rev. Lett.* **118**, 266101 (2017).
- [14] E. Prada, P. San-Jose, and L. Brey, *Phys. Rev. Lett.* **105**, 106802 (2010).
- [15] R. Podila, R. Rao, R. Tsuchikawa, M. Ishigami, and A. M. Rao, *ACS Nano* **6**, 5784 (2012).
- [16] F. Pizzocchero, L. Gammelgaard, B. S. Jessen, J. M. Caridad, L. Wang, J. Hone, P. Boggild, and T. J. Booth, *Nat. Commun.* **7**, 11894 (2016).
- [17] S. Deng and V. Berry, *Mater. Today* **19**, 197 (2016).
- [18] F. Guinea, M. I. Katsnelson, and A. K. Geim, *Nat. Phys.* **6**, 30 (2010).
- [19] R. J. Dolleman, D. Davidovikj, S. J. Cartamil-Bueno, H. S. J. van der Zant, and P. G. Steeneken, *Nano Lett.* **16**, 568 (2016).
- [20] S. P. Koenig, L. Wang, J. Pellegrino, and J. S. Bunch, *Nat. Nanotechnol.* **7**, 728 (2012).
- [21] F. Schedin, A. K. Geim, S. V. Morozov, E. W. Hill, P. Blake, M. I. Katsnelson, and K. S. Novoselov, *Nat. Mater.* **6**, 652 (2007).
- [22] J. S. Bunch, A. M. van der Zande, S. S. Verbridge, I. W. Frank, D. M. Tanenbaum, J. M. Parpia, H. G. Craighead, and P. L. McEuen, *Science* **315**, 490 (2007).
- [23] C. Chen, S. Rosenblatt, K. I. Bolotin, W. Kalb, P. Kim, I. Kymissis, H. L. Stormer, T. F. Heinz, and J. Hone, *Nat. Nanotechnol.* **4**, 861 (2009).
- [24] M. López-Suárez, R. Rurali, L. Gammaitoni, and G. Abadal, *Phys. Rev. B* **84**, 161401(R) (2011).
- [25] C. Ortix, S. Kiravittaya, O. G. Schmidt, and J. van den Brink, *Phys. Rev. B* **84**, 045438 (2011).

- [26] A. A. P. Sanjuan, M. Mehboudi, E. Harriss, H. Terrones, and S. Barraza-Lopez, *ACS Nano* **8**, 1136 (2014).
- [27] W. Helfrich, *Z. Naturforsch. C* **28**, 693 (1973).
- [28] R. Lipowsky, *Nature (London)* **349**, 475 (1991).
- [29] P. Koskinen and O. O. Kit, *Phys. Rev. B* **82**, 235420 (2010).
- [30] Y. Wei, B. Wang, J. Wu, R. Yang, and M. L. Dunn, *Nano Lett.* **13**, 26 (2013).
- [31] E. Abbena, S. Salamon, and A. Gray, *Modern Differential Geometry of Curves and Surfaces with Mathematica* (CRC Press, Boca Raton, 2006).
- [32] S. P. Timoshenko and S. Woinowsky-Krieger, *Theory of Plates and Shells* (McGraw-Hill, New York, 1959).
- [33] L. D. Landau and E. M. Lifshitz, *Theory of Elasticity* (Butterworth-Heinemann, Oxford, UK, 1999).
- [34] Y. Huang, J. Wu, and K. C. Hwang, *Phys. Rev. B* **74**, 245413 (2006).
- [35] D.-B. Zhang, E. Akatyeva, and T. Dumitrică, *Phys. Rev. Lett.* **106**, 255503 (2011).
- [36] C. Lee, X. Wei, J. W. Kysar, and J. Hone, *Science* **321**, 385 (2008).
- [37] D. Davidovikj, F. Alijani, S. J. Cartamil-Bueno, H. S. J. van der Zant, M. Amabili, and P. G. Steeneken, *Nat. Commun.* **8**, 1253 (2017).
- [38] K. N. Kudin, G. E. Scuseria, and B. I. Yakobson, *Phys. Rev. B* **64**, 235406 (2001).
- [39] B. Sajadi, S. van Hemert, B. Arash, P. Belardinelli, P. G. Steeneken, and F. Alijani, *Carbon* **139**, 334 (2018).
- [40] Q. Lu, M. Arroyo, and R. Huang, *J. Phys. D: Appl. Phys.* **42**, 102002 (2009).
- [41] R. Nicklow, N. Wakabayashi, and H. G. Smith, *Phys. Rev. B* **5**, 4951 (1972).
- [42] Y. W. Sun, W. Liu, I. Hernandez, J. Gonzalez, F. Rodriguez, D. J. Dunstan, and C. J. Humphreys, *Phys. Rev. Lett.* **123**, 135501 (2019).
- [43] F. Ahmadpoor, P. Wang, R. Huang, and P. Sharma, *J. Mech. Phys. Solids*. **107**, 294 (2017).
- [44] M. Zelisko, F. Ahmadpoor, H. Gao, and P. Sharma, *Phys. Rev. Lett.* **119**, 068002 (2017).
- [45] G. Bouglet, C. Ligoure, A. M. Bellocq, E. Dufourc, and G. Mosser, *Phys. Rev. E* **57**, 834 (1998).
- [46] H.-T. Jung, S. Y. Lee, and J. A. Zasadzinski, *Proc. Natl. Acad. Sci. USA* **99**, 15318 (2002).
- [47] S. Semrau, T. Idema, L. Holtzer, T. Schmidt, and C. Storm, *Phys. Rev. Lett.* **100**, 088101 (2008).
- [48] M. Ashino, K. Nishioka, K. Hayashi, and R. Wiesendanger, *Phys. Rev. Lett.* **126**, 146101 (2021).
- [49] M. Ashino, A. Schwarz, T. Behnke, and R. Wiesendanger, *Phys. Rev. Lett.* **93**, 136101 (2004).
- [50] G. Binnig, C. F. Quate, and C. Gerber, *Phys. Rev. Lett.* **56**, 930 (1986).
- [51] S. Morita, F. Giessibl, E. Meyer, and R. Wiesendanger, *Noncontact Atomic Force Microscopy* (Springer, Switzerland, 2015), Vol. 3.
- [52] M. Ashino and R. Wiesendanger, *Sci. Rep.* **7**, 46083 (2017).
- [53] V. Vitelli and A. M. Turner, *Phys. Rev. Lett.* **93**, 215301 (2004).
- [54] R. C. Haddon, *Science* **261**, 1545 (1993).
- [55] M. Haluška, M. Hulman, B. Hornbostel, J. Čech, V. Skákalová, and S. Roth, *Phys. Status Solidi B* **243**, 3042 (2006).
- [56] A. Thess *et al.*, *Science* **273**, 483 (1996).
- [57] W. Allers, A. Schwarz, U. D. Schwarz, and R. Wiesendanger, *Rev. Sci. Instrum.* **69**, 221 (1998).
- [58] Silicon Cantilever SSS-NCL, NANOSENSORS™, Switzerland.
- [59] T. R. Albrecht, P. Grütter, D. Horne, and D. Rugar, *J. Appl. Phys.* **69**, 668 (1991).
- [60] S. Morita, R. Wiesendanger, and E. Meyer, *Noncontact Atomic Force Microscopy: NanoScience and Technology* (Springer, Berlin, 2002).
- [61] W. N. Sharpe Jr., *Springer Handbook of Experimental Solid Mechanics*, Springer Handbooks (Springer US, 2008).
- [62] M. Ashino, D. Oberfell, M. Haluška, S. Yang, A. N. Khlobystov, S. Roth, and R. Wiesendanger, *Nat. Nanotechnol.* **3**, 337 (2008).
- [63] M. Ashino and R. Wiesendanger, *Jpn. J. Appl. Phys.* **45**, 2286 (2006).
- [64] M. Ondráček, P. Pou, V. Rozsival, C. González, P. Jelínek, and R. Pérez, *Phys. Rev. Lett.* **106**, 176101 (2011).
- [65] V. Meunier and P. Lambin, *Phys. Rev. Lett.* **81**, 5588 (1998).
- [66] D. V. Kosynkin, A. L. Higginbotham, A. Sinitskii, J. R. Lomeda, A. Dimiev, K. B. Price, and J. M. Tour, *Nature (London)* **458**, 872 (2009).
- [67] See Supplemental Material at <http://link.aps.org/supplemental/10.1103/PhysRevB.104.085407> for  $z$ -height images, interatomic forces, and AFM-image analyses, which include Refs. [77,78].
- [68] M. K. Kostov, H. Cheng, A. C. Cooper, and G. P. Pez, *Phys. Rev. Lett.* **89**, 146105 (2002).
- [69] C. Kittel, *Introduction to Solid State Physics*, 6th ed. (John Wiley & Sons, Inc., New York, U.S.A., 1986).
- [70] M. L. Colussi, L. Neves, and R. Baierle, *Braz. J. Phys.* **36**, 886 (2006).
- [71] M.-F. Yu, T. Kowalewski, and R. S. Ruoff, *Phys. Rev. Lett.* **85**, 1456 (2000).
- [72] X. Blase, L. X. Benedict, E. L. Shirley, and S. G. Louie, *Phys. Rev. Lett.* **72**, 1878 (1994).
- [73] E.-A. Kim and A. H. C. Neto, *Europhys. Lett.* **84**, 57007 (2008).
- [74] M. Ashino and R. Wiesendanger, *Crystals* **8**, 102 (2018).
- [75] M. K. Bleses, A. W. Barnard, P. A. Rose, S. P. Roberts, K. L. McGill, P. Y. Huang, A. R. Ruyack, J. W. Kevek, B. Kobrin, D. A. Muller, and P. L. McEuen, *Nature (London)* **524**, 204 (2015).
- [76] B. F. Grosso and E. J. Mele, *Phys. Today* **73**(9), 46 (2020).
- [77] H. Hölscher, U. D. Schwarz, and R. Wiesendanger, *Appl. Surf. Sci.* **140**, 344 (1999).
- [78] J. E. Sader and S. P. Jarvis, *Appl. Phys. Lett.* **84**, 1801 (2004).